Opto-Electronics Review

journal homepage: https://journals.pan.pl/opelre

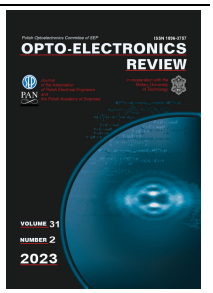

Theoretical study of back-to-back avalanche photodiodes for dual-band infrared applications

Tetiana Manyk*, Kinga Majkowycz, Jarosław Rutkowski, Piotr Martyniuk

Institute of Applied Physics, Military University of Technology, gen. Sylwestra Kaliskiego 2, 00-908 Warsaw, Poland

Article info

Article history:
Received 28 Nov. 2022
Received in revised form 08 Mar. 2023
Accepted 08 Mar. 2023
Available on-line 05 May 2023

Keywords:
IR detectors;
HgCdTe avalanche photodiodes;
excess noise;
gain;
dual-band detectors.

Abstract

The dual-band avalanche photodiode (APD) detector based on a HgCdTe material system was designed and analysed in detail numerically. A theoretical analysis of the two-colour APD intended for the mid wavelength infrared (MWIR) and long wavelength infrared (LWIR) ranges was conducted. The main purpose of the work was to indicate an approach to select APD structure parameters to achieve the best performance at high operating temperatures (HOT). The numerical simulations were performed by *Crosslight* numerical APSYS platform which is designed to simulate semiconductor optoelectronic devices. The current-voltage characteristics, current gain, and excess noise analysis at temperature $T = 230$ K *vs*. applied voltage for MWIR ($U = 15$ V) and LWIR ($U = –6$ V) ranges were performed. The influence of low and high doping in both active layers and barrier on the current gain and excess noise is shown. It was presented that an increase of the APD active layer doping leads to an increase in the photocurrent gain in the LWIR detector and a decrease in the MWIR device. The dark current and photocurrent gains were compared. Photocurrent gain is higher in both spectral ranges.

1. Introduction

Mercury cadmium telluride (HgCdTe) has been a well-known semiconductor for many years, used in the fabrication of very sensitive detectors operating in a wide range of the infrared (IR) spectrum. The main advantages of this ternary alloy are a direct bandgap depending on the stoichiometric cadmium (Cd) composition (x), low dielectric constant, high electron mobility, and high possibility of controlling the level of charge carrier concentrations. An important feature enabling the high-quality structures to be grown is the extremely small change in the lattice constant with Cd composition. This feature enables the fabrication of detectors for detection of radiation of two different wavelengths, which allows the determination of the absolute temperature of the IR scene, assuming a constant emissivity in the entire spectral range [1–4]. Various device architectures were developed with the possibility of independent and simultaneous detection of radiation in two separate wave regions. Dual-band outputs can be accessed by designing a back-to-back diode structure. In this two-colour device architecture, the longer wavelength photodiode is placed behind the shorter wavelength one. Idea for the first multi-colour detector using HgCdTe was presented in the 1970s [5]. IR avalanche photodiodes (APDs) exhibit high gain and low noise. The HgCdTe is a well-suited semiconductor material for APDs applications due to the fact that a variable bandgap can be matched to the desired IR range [6–8]. In addition, the HgCdTe impact ionization coefficient $k = \alpha_h/\alpha_e$ is dependent on the Cd composition being presented in Fig. 1 [9]. The hole to electron ionization coefficient determines the semiconductor material ability for avalanche effect. According to Fig. 1, the hole ionization is favourable for the short wavelength infrared (SWIR) HgCdTe detectors ($0.5 < x < 0.7$). The electron ionization is advantageous for the mid wavelength infrared (MWIR) and long wavelength infrared (LWIR) detectors ($x < 0.5$). Due to the law of conservation of both momentum and energy, a threshold energy, V_{th} requirement must be met by the primary carrier. This energy must be higher than the material bandgap (E_g) due to the fact that the carrier also undergoes non-ionizing collision processes such as phonon scattering.

*Corresponding author at: tetjana.manyk@wat.edu.pl

https://doi.org/10.24425/opelre.2023.145093
1896-3757/ Association of Polish Electrical Engineers (SEP) and Polish Academic of Sciences (PAS). Published by PAS

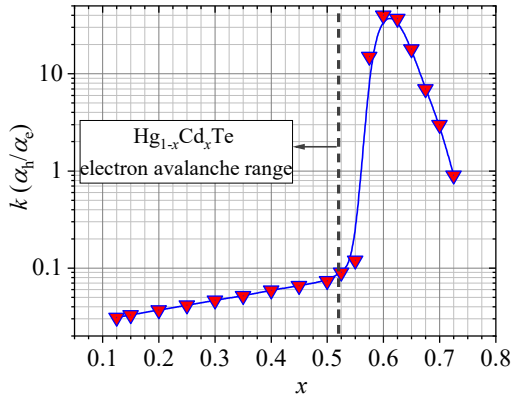

Fig. 1. The $k = \alpha_h/\alpha_e$ impact ionization coefficient *vs.* Cd composition dependence for $Hg_{1-x}Cd_xTe$ [9].

The pBp and nBn HgCdTe detectors typically operate at the bias voltage < 1 V. This bias is much lower than the voltage required for the avalanche process. APDs HgCdTe detectors are particularly useful in the low incident flux detection due to their excellent performance in low excess noise and high multiplication gain [10–12]. The sequential dual-band MWIR back-to-back HgCdTe photodiode with P-type separating barrier layer is the most promising two-colour detection structure. In a dual-band APD structure, the blocking barrier makes it possible to reduce the carrier concentration in the absorber area and decrease dark current. The first information about two-colour APD detectors was presented in 2006 [13]. That concerned the demonstration of a bi-colour-avalanche gain detection in HgCdTe FPA operating at 77 K. The cut-off wavelengths were 4.9 µm and 10 µm for the MWIR and LWIR diodes, respectively. An avalanche gain of $M = 5300$ at an inverse bias was reported for an MWIR wavelength diode. The design and simulation of a bias-selectable dual-band photodetector operating in the visible (VIS) and near infrared (NIR) regions research was also conducted [14]. The photodetector consisted of two back-to-back APDs with InGaAs and Si absorption layers, respectively.

The paper presents research on the APD structure with a blocking barrier ($x = 0.45$). The use of a barrier allows to reduce the carrier concentration in absorption areas. Theoretical simulations are based on the APSYS numerical platform (*Crosslight*) [15]. The APSYS package is designed to simulate semiconductor optoelectronic devices. It uses a finite element analysis in 2/3 dimensions and includes many advanced physical models such as hot carrier transport, heterojunction models, and thermal analysis. Theoretical simulation of the HgCdTe APDs was performed by numerical solving of the Poisson's and the electron/hole current continuity equations. The applied models incorporate both HgCdTe electrical and optical properties taking under consideration the radiative, Auger, Shockley-Read-Hall (SRH) generation-recombination (GR) processes. In this paper, the theoretical modelling of the dual-band N^+–p–p–p–P^+–p–p–p–n^+ back-to-back APDs was presented. It was shown how the two-colour photodiode would operate with an extra multiplication layer with similar to the active layer bandgap energies. The influence of the avalanche effect on the dark current density, gain and excess noise in the HgCdTe dual-band APDs was presented. The use of complex HgCdTe heterostructures with a desired composition and doping profiles allowed to design APD detectors intended to operate under higher operating temperature conditions (HOT) $T > 200$ K.

2. Avalanche photodiode structure and theoretical modelling approach

A simulated HgCdTe APD consists of two back-to-back photodiodes. The photodiodes operate in the MWIR and LWIR regions at $T = 230$ K, with cut-off wavelengths, $\lambda_{cut\text{-}off} = 4$ µm and 9 µm, respectively. Figure 2 shows the structure of the analysed detector and Table 1 lists the main parameters (type and level of doping, thicknesses and the Cd composition, x) of all individual layers designed in the order: CL/ML/AL/TL/BL/TL/AL/ML/CL (with abbreviations description below Table 1). It is worth noting that the multiplication layers were assumed to be p-type doped at a very low level (in the order of $p = 10^{14}$ cm^{-3}). An advantage of the back-to-back HgCdTe APD is simplicity of the device fabrication and simplification of the material growth process itself. The homogeneous composition of HgCdTe APD reduces defects at the interface of successive layers and thus reduces tunnel currents, thanks to which the analysed structures are characterised by higher homogeneity [9, 16].

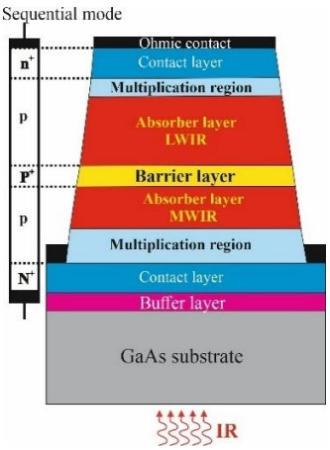

Fig. 2. The analysed dual-band, back-to-back APD structure.

Table 1.
Structural parameters used in the theoretical simulation of the APDs.

Region*	Doping concentration (cm^{-3})	Thickness (µm)	Cd composition
N^+-CL	$4.0 \cdot 10^{17}$	3	0.40
p-ML	$3.0 \cdot 10^{14}$	1	*grad* (0.40–0.33)
p-AL	$\mathbf{8.0 \cdot 10^{14}}$	**5**	**0.33**
p-TL	$8.0 \cdot 10^{15}$	0.1	*grad* (0.33–0.45)
P^+-BL	$1.0 \cdot 10^{17}$	0.3	0.45
p-TL	$1.0 \cdot 10^{15}$	0.1	*grad* (0.45–0.20)
p-AL	$\mathbf{2.0 \cdot 10^{15}}$	**7**	**0.20**
p-ML	$5.0 \cdot 10^{14}$	1	0.225
N^+-CL	$1.0 \cdot 10^{17}$	3	0.250

*The following abbreviations were introduced in the Table 1: Contact layer (CL); Multiplication layer (ML); Active layer (AL); Transient layer (TL); Barrier layer (BL).

The energy bandgap diagram of the theoretically simulated unbiased APDs structure is presented in Fig. 3. In this figure, the following was marked: E_c is the bottom edge of the conduction band, E_v is the top edge of the valence band, and $E_{F\_n(p)}$ is the Fermi level. For unbiased condition, a barrier in the valence band is visible what can be reduced by assuming a high doping in the barrier layer.

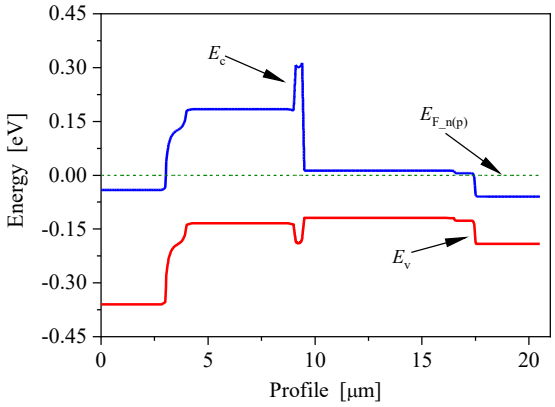

Fig. 3. Energy band structure *vs.* APD profile (unbiased condition).

The photodiode parameters were analysed with and without impact ionization in active and multiplication layers. Impact ionization is defined through the expression for the generation rate

$$G = \frac{\alpha_e J_{ne}}{q} + \frac{\alpha_h J_h}{q}, \tag{1}$$

where q is the elementary charge, J_e and J_h are the current densities (electrons and holes appropriately).

The Chynoweth model [15, 17] was used to determine the electrons and holes ionization coefficient by equations:

$$\alpha_e = a_e e^{\frac{-b_e}{F}}, \tag{2}$$

$$\alpha_h = a_h e^{\frac{-b_h}{F}}, \tag{3}$$

where F is the electric field in the multiplication region and the coefficients $a_e = 6.9 \cdot 10^4\ \mathrm{cm}^{-1}$ and $a_h = 6.9 \cdot 10^2\ \mathrm{cm}^{-1}$ for the MWIR range, and $a_e = 6.0 \cdot 10^4\ \mathrm{cm}^{-1}$, and $a_h = 6.0 \cdot 10^2\ \mathrm{cm}^{-1}$ for the LWIR range, but the critical fields b_e and b_h were equal $3.7 \cdot 10^4$ V/cm for both operating wavelengths. The ionization coefficient $k = 0.01$ (holes to electrons ratio) was used to investigate the effect of the absorber doping level on the tested APDs current-voltage (J_d-V) characteristics.

For APD performance simulations, the following Auger GR coefficients were used: F_{12}(LWIR range) = 0.25 ($\gamma = 5$), F_{12}(MWIR range) = 0.20 ($\gamma = 5$) and SRH lifetime: τ_n(LWIR range) = 15 ns, τ_p(LWIR range) = 1.5 ns, τ_n(MWIR range) = 120 ns, and τ_p(MWIR range) = 12 ns.

The simulated APD operates in sequential mode. By switching the bias voltage from a positive to negative value, it is possible to detect the signal in the first peak wavelength ($\lambda_{Peak} = 3.4$ μm) or the second absorber ($\lambda_{Peak} = 6.5$ μm). Figure 4 shows how the band structure changes under the influence of positive and negative polarization. Theoretical modelling is performed for the

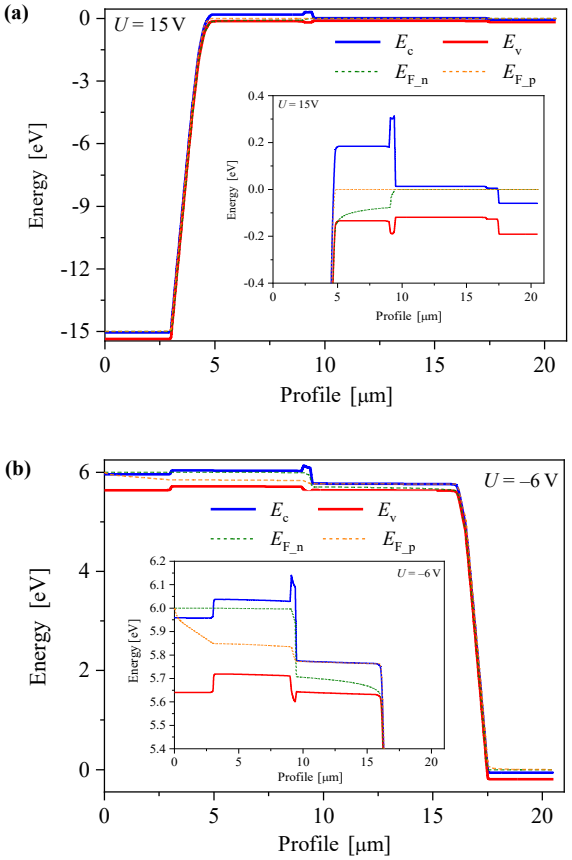

Fig. 4. Energy band structure *vs.* APD profile: (a) forward bias ($U = 15$ V), (b) reverse bias ($U = -6$ V).

bias range from $U = +15$ V to $U = -6$ V. For forward bias, all voltage drops at the MWIR junction, and for reverse bias at the LWIR junction. Insets in Fig. 4 present the magnified absorber areas to show the position of the Fermi levels in relation to the energy bands.

The simulated dark current density (J_d) is presented in Fig. 5. Dependence of dark current density as a function of bias for the tested two-colour APD with and without impact ionization has been shown. With positive polarization, the MWIR junction is polarized in the reverse and LWIR in the forward direction, while in the case of negative polarization, it is opposite. The current density for the LWIR detector is more than three orders of magnitude higher than the saturation current for the MWIR detector.

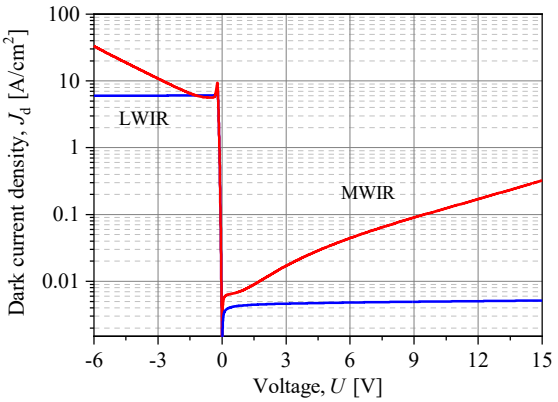

Fig. 5. Dark current density (J_d) as a function of voltage with (red curve) and without (blue curve) impact ionization.

Gain is a parameter that describes the impact ionization level. APD requires high internal gain with low noise and high bandwidth for detection and amplification of attenuated optical signals. The dark current and photocurrent gains were compared. The APD dark current gain was defined as the ratio of the dark current with and without impact ionization determined by (4).

$$M(V) = \frac{J_{\text{dark with ii}}(V)}{J_{\text{dark without ii}}(V)} . \tag{4}$$

The photocurrent avalanche gain was extracted by (5). It is the ratio of the difference between photo and dark currents at a given voltage to that difference at zero bias.

$$M_{\text{ph}}(V) = \frac{J_{\text{ph}}(V) - J_{\text{dark}}(V)}{J_{\text{ph}}(V=0) - J_{\text{dark}}(V=0)} . \tag{5}$$

When determining the photocurrent gain, the structure was illuminated from the MWIR detector side with a 100 W/m^2 radiation with a wavelength of 3 µm and 6 µm corresponding to the maximum sensitivity of the MWIR and LWIR absorbers, respectively.

The noise in the APD is related to the fluctuations of the charge carriers generated by photons and associated with thermally generated dark currents. The excess noise is generated by the fluctuation of the charge carriers produced by the photons and the magnitude (I_S) is given by

$$I_S^2 = 2qI_{\text{ph}}M^2F(M), \tag{6}$$

where M is the avalanche photo gain, $F(M)$ is the excess noise factor, and I_{ph} is the photocurrent. Excess noise is a consequence of statistical fluctuation in the multiplication process. The excess noise factor $F_e(M)$ for pure electron injection is defined as [9]

$$F_e(M) = M\left[1 - (1-k)\left[\frac{M-1}{M}\right]^2\right]. \tag{7}$$

For better APD performance, i.e., high internal gain with low noise and high bandwidth for detection and amplification of attenuated optical signals, both dark current and excess noise should be minimized.

3. Results and discussion

The photocurrent gain M and noise factor $F_e(M)$ for the analysed two-colour APDs are presented in Fig. 6. The photocurrent gain increases *vs*. bias voltage, but much slower than in the case of one-colour APDs. The excess noise factor $F_e(M)$ for pure electron injection at low voltages rises faster than gain and then saturates.

Figure 7 shows the gain of dark current and photocurrent *vs*. bias for the MWIR and LWIR ranges. The photocurrent gain was always higher than the dark current one. The difference between the dark and photocurrent gain increases when the doping in the MWIR absorber increases and in the LWIR active layer decreases.

Figure 8 presents the gain and excess noise factor $F(M)$ *vs*. acceptor concentration in the absorber layers. Doping changes in the active layers affect the LWIR and

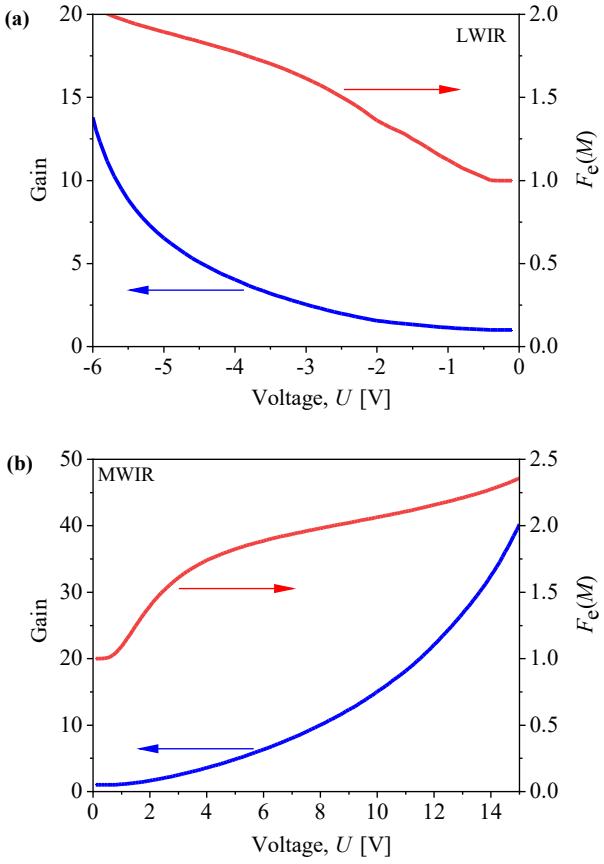

Fig. 6. Photocurrent gain and excess noise factor for the LWIR (a) and MWIR (b) ranges *vs*. voltage.

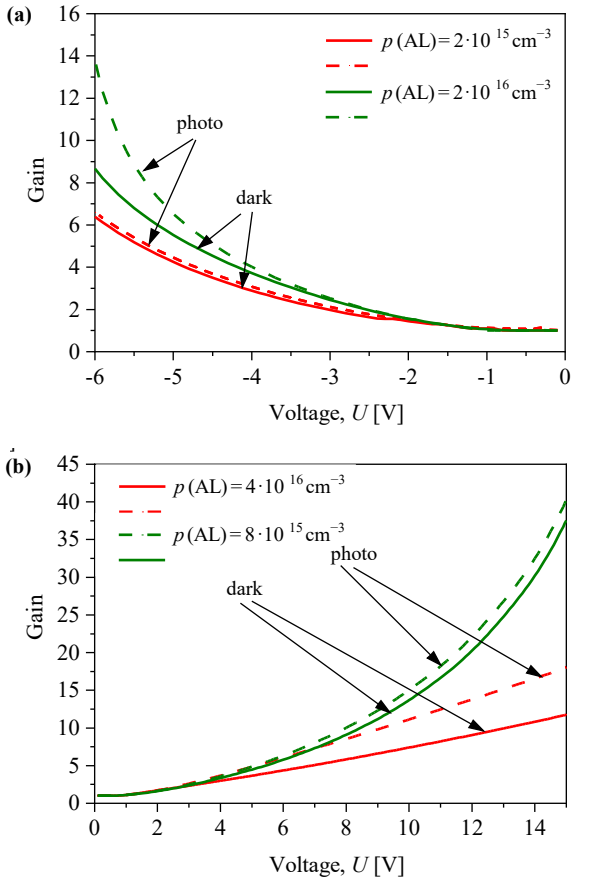

Fig. 7. Dark and photocurrent gain for the LWIR (a) and MWIR (b) ranges *vs*. voltage for the selected doping levels in AL.

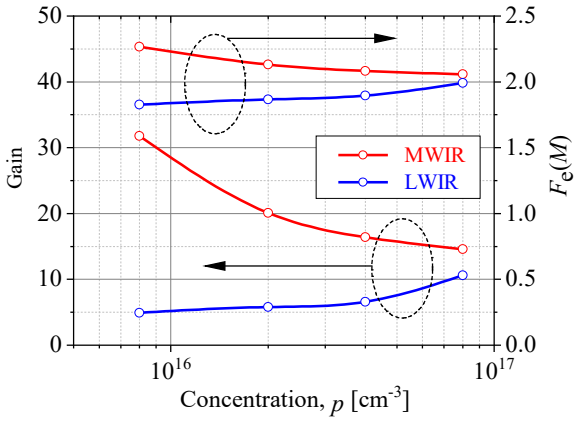

Fig. 8. Photocurrent gain and excess noise factor for the MWIR ($U = +14$ V) and LWIR ($U = -5$ V) range *vs*. absorber concentrations.

MWIR detectors gains differently. The LWIR detector gain increases *vs*. doping, while the MWIR detector gain decreases. In order to explain this effect, the influence of the absorbers doping on the electric field distribution and the carriers GR rates was investigated.

Figure 9 shows the electric field distribution *vs*. APD profile and voltage polarization. The electric field in multiplication layers is more than two orders higher than in absorbers. For both MWIR and LWIR junctions, the electric field increases in the multiplication region *vs*. absorbers doping contributing to the higher gains.

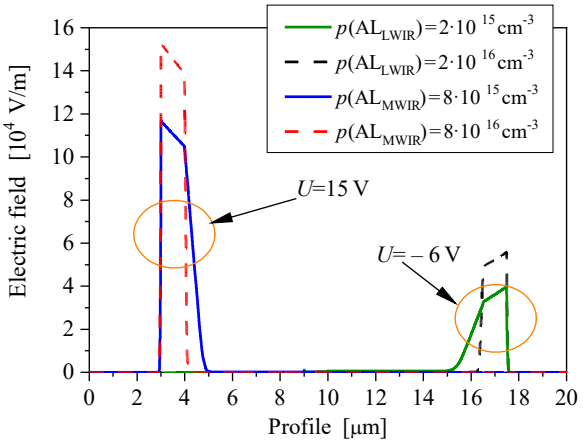

Fig. 8. Electric field *vs*. APD profile for the selected levels of absorbers doping and voltage polarization.

Figure 10 shows the influence of absorber doping on Auger, radiative and SRH GR rates of carriers. For the low doping concentration in the LWIR and MWIR absorbers, the SRH recombination predominates Auger processes. An increase of doping in the LWIR absorber leads to a sharp increase in Auger recombination what contributes to higher gains. On the other hand, for the MWIR absorber, the rate of predominant SRH recombination decreases and lower gains are observed what was presented in Fig. 8.

The introduction of a doping change in the multiplication layer does not affect the current gain. The barrier doping influence on gain in the MWIR and LWIR APDs is presented in Fig. 11. It can be seen that an increase in the p-type doping causes a decrease in the photo gain in the LWIR detector. The MWIR device is not sensitive to

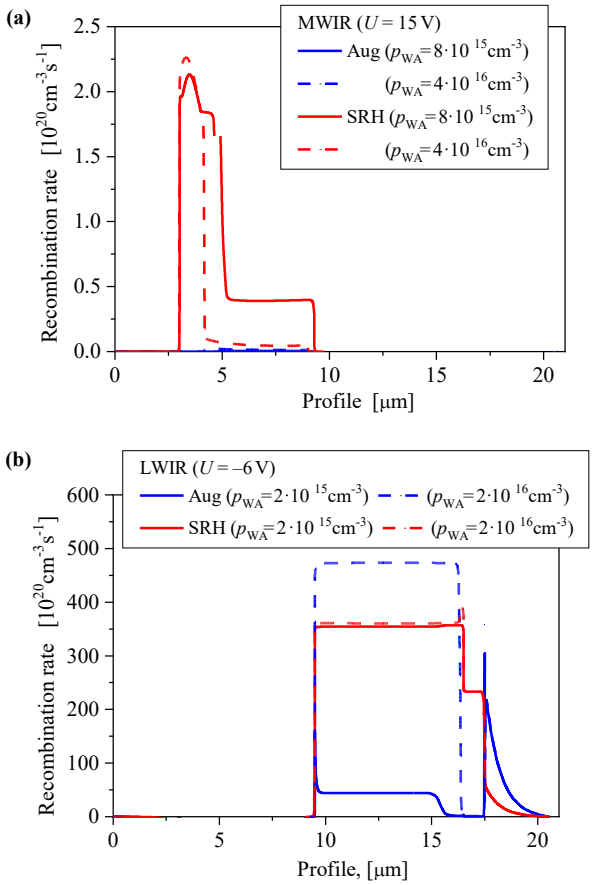

Fig. 10. Recombination rate for the MWIR (a) and LWIR (b) APD junctions *vs*. profile for the selected levels of the absorber doping.

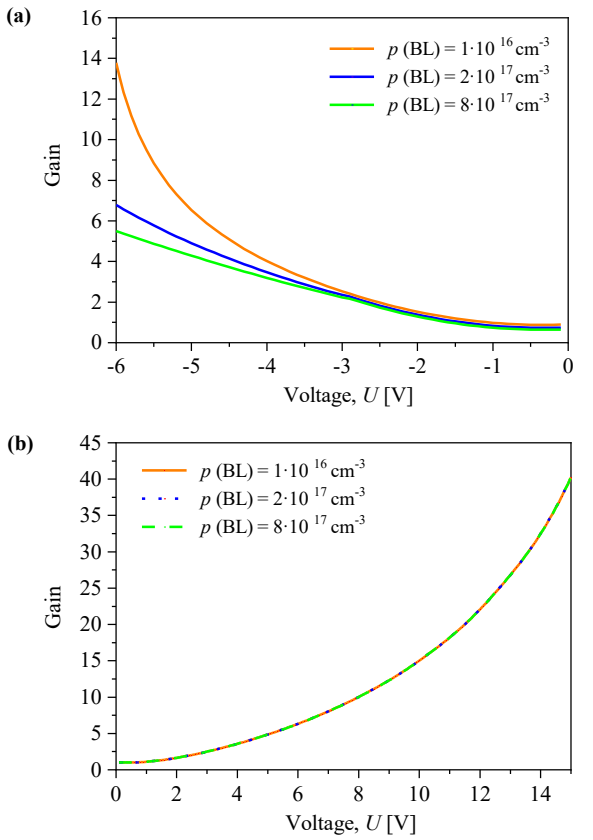

Fig. 11. Photocurrent gain for the LWIR (a) and MWIR (b) junction as a function of voltage for three selected levels of doping in the barrier layer.

doping changes in the barrier layer, because SRH recombination dominates in this range and its rate does not depend on the barrier parameters.

In the analysed structure, as in any two-colour detector, crosstalk between the bands arises (see Fig. 12). In our case, the crosstalk for the MWIR detector is negligible, while for the LWIR detector is much higher (2.5%).

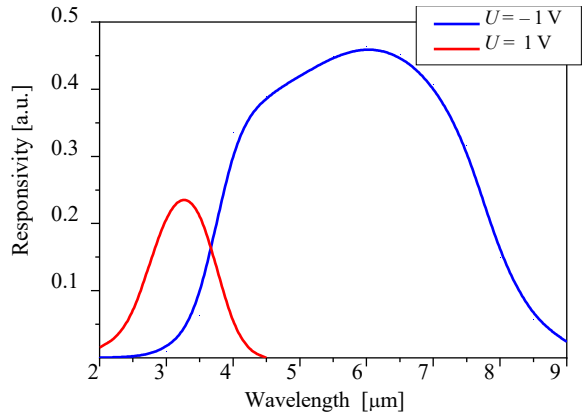

Fig. 12. Responsivity for the LWIR and MWIR junction as a function of wavelength.

This is due to the fact that not all the $\lambda = 3$ μm radiation is absorbed in the MWIR absorber and some of it reaches the second detector. Figure 13 shows the optical generation of carriers in the APD structure when illuminated by IR with a wavelength $\lambda = 3$ μm and 6 μm.

The barrier separating the two detectors determines the low level of crosstalk on the MWIR detector.

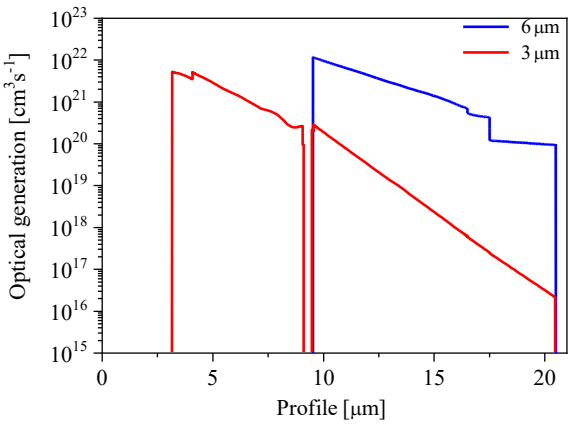

Fig. 13. Optical generation rate *vs*. layer thickness of the back-to-back detector.

4. Conclusions

The dual-band HgCdTe APD structure was numerically analysed. The two back-to-back photodiodes operating in the MWIR and LWIR regions at $T = 230$ K were sequentially activated by changing the polarity from 15 V to −6 V, respectively. The photocurrent gain was slightly higher than the dark current gain. The gain value for the LWIR detector reaches 10 while for the MWIR active layer is about 40. For the LWIR detector, an increase in gain was observed *vs*. doping concentration in the absorber, whereas in the MWIR detector the situation is opposite. The explanation for this fact is the strong suppression of Auger recombination in the LWIR structure at low carrier concentrations. It was shown that the change in the doping concentration in barrier separating junctions of the two-colour detector does not affect the gain in the MWIR detector, but significantly changes the gain in the LWIR device. This is due to the fact that the SRH recombination dominates in the MWIR junction, while Auger processes are more important in the LWIR region.

The signal crosstalk is much higher for the LWIR structure due to an incomplete absorption of the shortwave radiation in the MWIR region.

Authors' statement

Research concept and design, P.M. and J.R.; collection and/or assembly of data, K.M.; data analysis and interpretation, T.M.; writing the article, T.M. and J.R.; critical revision of the article, P.M.; final approval of article, P.M. and J.R.

Acknowledgements

This research was funded by The National Science Centre, Poland – grant no. UMO-2019/33/B/ST7/00614.

References

[1] Plis, E. A., Krishna, S. S., Gautam, N. & Wyers, S. Bias switchable dual-band InAs/GaSb superlattice detector with pBp architecture. *IEEE Photon. J.* **3**, 234–240 (2011). https://doi.org/10.1109/JPHOT.2011.2125949

[2] Rutkowski, J. *et al*. Two-colour HgCdTe infrared detectors operating above 200K. *Opto-Electron. Rev.* **16**, 321–327 (2008). https://doi.org/10.2478/s11772-008-0023-2

[3] Hu, W. *et al*. 128×128 long-wavelength/mid-wavelength two-color HgCdTe infrared focal plane array detector with ultralow spectral cross talk. *Opt. Lett.* **39**, 5184–5187 (2014). https://doi.org/10.1364/OL.39.005184

[4] Rhiger, D. R. & Bangs, J. W. Current-voltage analysis of dual-band n-p-n HgCdTe detectors. *J. Electron. Mater.* **51,** 4721–4730 (2022). https://doi.org/10.1007/s11664-022-09803-4

[5] Halpert, H. & Musicant, B. L. N-color (Hg,Cd)Te photodetectors. *Appl. Opt.* **11**, 2157–2161 (1972). https://doi.org/10.1364/AO.11.002157

[6] Beck, J. *et al*. The HgCdTe electron avalanche photodiode. *J. Electron. Mater.* **35**, 1166–1173 (2006). https://doi.org/10.1007/s11664-006-0237-3

[7] He, J. *et al*. Design of a bandgap-engineered barrier-blocking HOT HgCdTe long-wavelength infrared avalanche photodiode. *Opt. Express* **28**, 33556–33563 (2020). https://doi.org/10.1364/OE.408526

[8] Rogalski, A. HgCdTe infrared detector material: history, status and outlook. *Rep. Prog. Phys.* **68**, 2267–2336(2005). https://doi.org/10.1088/0034-4885/68/10/R01

[9] Singh, A., Srivastav, V. & Pal, R. HgCdTe avalanche photodiodes A review. *Opt. Laser Technol.* **43**, 1358–1370 (2011). https://doi.org/10.1016/j.optlastec.2011.03.009

[10] Kopytko, M., Sobieski, J., Xie, R., Jozwikowski, K. & Martyniuk, P. Impact ionization in HgCdTe avalanche photodiode optimized to 8 μm cut-off wavelength at 230 K. *Infrared Phys. Technol.* **115**, 103704 (2021). https://doi.org/10.1016/j.infrared.2021.103704

[11] Levaquet, G., Nasser, M., Bertho, D., Orsal, B. & Alabedra, R. Ionization energies in $Cd_xHg_{1-x}Te$ avalanche photodiodes. *Semicond. Sci. Technol.* **8**, 1317–1323 (1993). https://doi.org/10.1088/0268-1242/8/7/021

[12] Kinch, M., Beck, J. D., Wan, C. F., Ma, F. & Campebell, J. HgCdTe electron avalanche photodiodes. *J. Electron. Mater.***33**, 630–639 (2004). https://doi.org/10.1007/s11664-004-0058-1

[13] Perrais, G, *et al*. Demonstration of multifunctional bi-colour-avalanche gain detection in HgCdTe FPA. *Proc. SPIE* **6395**, 63950H (2006). https://doi.org/10.1117/12.692689

[14] Cao, L., Hou, Y. & Zhang, L. Design and simulation of bias selectable few photon dual-colour photodetector operating in visible and near infrared regions. *Optoelectron. Lett.* **16**, 0333–0337 (2020). https://doi.org/10.1007/s11801-020-9165-3

[15] Crosslight Device Simulation Software – General Manual 2019 version. *Crossligth Software Inc*. (2019). https://crosslight.com/

[16] Osaka, F., Mikawa, T. & Kaneda, T. Impact ionization coefficient of the electrons and holes in (100)-oriented $Ga_{1-x}In_xAs_yP_{1-y}$. *IEEE J. Quantum Electron.* **21**, 1326–1338 (1985). https://doi.org/10.1109/JQE.1985.1072835

[17] Kinch, M. A. *Fundamentals of Infrared Detectors Materials*. (SPIE Press, Bellingham, Washington, 2007).